

A *Gaia* view of the two OB associations Cygnus OB2 and Carina OB1: The signature of their formation process

Beomdu Lim^{1,2,3*}, Yaël Nazé^{2†}, Eric Gosset^{2‡}, and Gregor Rauw²

¹*School of Space Research, Kyung Hee University, 1732 Deogyong-daero, Giheung-gu, Yongin-si, Gyeonggi-do 17104, Republic of Korea*

²*Space sciences, Technologies and Astrophysics Research Institute, Université de Liège, Quartier Agora, Allée du 6 Août 19c, Bât. B5c, 4000, Liège, Belgium*

³*Department of Astronomy and Space Science, Sejong University, 209 Neungdong-ro, Gwangjin-gu, Seoul 05006, Republic of Korea*

Accepted XXX. Received YYY; in original form ZZZ

ABSTRACT

OB associations are the prime star forming sites in galaxies. However the detailed formation process of such stellar systems still remains a mystery. In this context, identifying the presence of substructures may help tracing the footprints of their formation process. Here, we present a kinematic study of the two massive OB associations Cygnus OB2 and Carina OB1 using the precise astrometry from the *Gaia* Data Release 2 and radial velocities. From the parallaxes of stars, these OB associations are confirmed to be genuine stellar systems. Both Cygnus OB2 and Carina OB1 are composed of a few dense clusters and a halo which have different kinematic properties: the clusters occupy regions of 5–8 parsecs in diameter and display small dispersions in proper motion, while the halos spread over tens of parsecs with a 2–3 times larger dispersions in proper motion. This is reminiscent of the so-called “line width-size” relation of molecular clouds related to turbulence. Considering that the kinematics and structural features were inherited from those of their natal clouds would then imply that the formation of OB associations may result from structure formation driven by supersonic turbulence, rather than from the dynamical evolution of individual embedded clusters.

Key words: stars: formation – stars: kinematics and dynamics – open clusters and associations: individual (Cygnus OB2 and Carina OB1)

1 INTRODUCTION

OB associations are huge stellar systems incubating loose groups of O- and B-type stars spread over tens of parsecs (Ambartsumian 1947). These stellar systems are the pre-vailing star forming sites in external galaxies as well as in the Galaxy (Regan & Wilson 1993; Bresolin et al. 1996; Pietrzyński et al. 2001; Garcia et al. 2009), and they are considered as the birth places of field stars (Miller & Scalo 1978; Briceño et al. 2007). In addition, OB associations play a crucial role in the chemical evolution of host galaxies as massive stars in those associations produce heavy elements through supernova explosions. Despite their importance, our knowledge of such objects remains incomplete, in particular the details of their formation process are still not fully established. There are two main models concerning the origin

of OB associations, 1) the expansion of embedded clusters and 2) the formation of unbound stellar groups in-situ.

The majority of the stars in star forming regions are thought to form in clusters (Lada & Lada 2003; Porras et al. 2003; Koenig et al. 2008), but only less than 10 per cent of these clusters can remain bound, according to comparison of the observed number of clusters with the predictions of a model for a constant cluster formation rate (Lada & Lada 2003). Most cluster members are then scattered out after gas expulsion (Lada et al. 1984; Kroupa et al. 2001; Baumgardt & Kroupa 2007). The role of rapid gas expulsion in disruption of star clusters was studied by several groups (Tutukov 1978; Hills 1980; Goodwin & Bastian 2006). This dynamical evolution leads to the formation of unbound OB associations.

According to the second model, the origin of OB associations can be explained by star formation taking place in hierarchical substructures of molecular clouds. Shocks by turbulent flows can create a network of a number of substructures inside a molecular cloud (Larson 1981; Padoan

* Corresponding author, E-mail: blim@khu.ac.kr

† Research Associate FRS-FNRS (Belgium)

‡ Research Director FRS-FNRS (Belgium)

et al. 2001; Elmegreen 2002). Both bound clusters and distributed population of stars form along these substructures with different sizes and densities. Bound clusters preferentially form in high-density regions because such regions have high-star formation efficiency, while low-density regions with low-star formation efficiency form distributed stellar populations (Bonnell et al. 2011; Kruijssen 2012). Gas pressure is also a considerable factor to form either bound clusters or sparse groups of stars (Elmegreen 2008).

A number of observational studies have attempted to understand the dynamical evolution of OB associations and eventually their formation process (Wright et al. 2016; Mel'nik & Dambis 2017; Cantat-Gaudin et al. 2018; Kounkel et al. 2018; Ward & Kruijssen 2018; Wright & Mamajek 2018; Kuhn et al. 2019). Many OB associations seem to be unbound, given that their total stellar masses are smaller than virial masses (Mel'nik & Dambis 2017). The Orion Molecular Cloud Complex hosts about 190 subgroups of stars, which are associated with five main components composing this complex (Kounkel et al. 2018). One of them, the gas-deficient component Orion D (see Kounkel et al. 2018 for details), exhibits a pattern of expansion. Cantat-Gaudin et al. (2018) also found non-isotropic expansion of stellar subgroups in the direction of the Vela-Puppis region. The ages of these subgroups exceed the dissipation timescale (10 Myr) of molecular clouds around open clusters (Leisawitz et al. 1989). There may be little molecular gas around the subgroups. The origin of gas-deficient OB associations could be explained by the model of expansion of embedded clusters after rapid gas expulsion.

On the other hand, Wright & Mamajek (2018) could not find evidence for global expansion in the Scorpius-Centaurus OB association, but they found that this association is highly substructured. Ward & Kruijssen (2018) investigated 18 nearby OB associations using the Tycho-*Gaia* Astrometric Solution data (Michalik et al. 2015). They also could not find any signature of global expansion from a single cluster or multiple clusters. Cantat-Gaudin et al. (2018) claimed that the anisotropic expansion and the complicated star formation history among the unbound subgroups of stars in the Vela-Puppis region may be the footprints of structure formation inside molecular clouds driven by turbulent flows.

Up to today, a number of previous studies have reported different dynamical status for various OB associations. Hence, more conclusive evidence for each theoretical model is still required to find a suitable explanation for their origin. The recent high-precision astrometry from the *Gaia* mission (Gaia Collaboration et al. 2016) opens a new window for addressing this issue. In this paper, we use the recent astrometric data from the Gaia Data Release 2 (DR2; Gaia Collaboration et al. 2018) to test the two proposed models for the two massive OB associations Cygnus OB2 (Cyg OB2) and Carina OB1 (Car OB1).

Cyg OB2 is the most massive nearby OB association. This association contains an abundant population of O- and B-type stars (Johnson & Morgan 1954; Massey & Thompson 1991; Comerón et al. 2002; Walborn et al. 2002; Hanson 2003; Kiminki et al. 2007, etc.) with a total mass reaching about $2\text{--}10 \times 10^4 M_\odot$ (Knödseder 2000; Wright et al. 2010, 2015). The distance to Cyg OB2 was thought to be about $d = 1.4$ kpc (Hanson 2003; Rygl et al. 2012), but the association is severely obscured by dust lanes, leading

to high levels of extinction ($A_V = 4\text{--}20$ mag, Knödseder 2000; Wright et al. 2015). Extensive studies of this association showed that Cyg OB2 is gravitationally unbound and highly substructured with different kinematics (Wright et al. 2014, 2016). However, no evidence for an overall expanding motion of stars was found. Accordingly, Wright et al. (2014, 2016) claimed that Cyg OB2 has not originated from the expansion of a single star cluster. Berlanas et al. (2019) explored the internal substructures of these associations using the parallaxes from *Gaia* DR2 and found that two stellar groups are lying along the line-of-sight. Kiminki et al. (2007) measured the radial velocities (RVs) of OB stars in this association, but they could not find any spatial variation of RVs.

Car OB1 association is one of the most active star forming complexes in the Carina-Sagittarius spiral arm. This association is supposed to be located at $2.2\text{--}2.9$ kpc (Allen & Hillier 1993; Smith 2006; Hur et al. 2012). It contains a large number of O- and B-type stars (Walborn 1973, 1995; Walborn et al. 2002; Levato & Malaroda, 1982; Morrell et al. 1988; Massey & Johnson, 1993), and its total mass exceeds $2 \times 10^4 M_\odot$ (Preibisch et al. 2011). Several star clusters, such as Trumpler 14 (Tr14), 15 (Tr15), 16 (Tr16), Bochum 10, 11, Collinder 232, and 228, as well as halo populations are distributed over this complex (Feigelson et al. 2011). However, it is still uncertain whether or not these clusters are part of the same association. Tr14, 16, and Collinder 232 have almost the same mean proper motions (PMs) within the measurement errors (Cudworth et al. 1993). In addition, the RVs of stars in the star clusters of Car OB1 reveal a single Gaussian distribution although there is a slight difference in RVs between Tr14 and Tr16 (Kiminki & Smith 2018). Thus, these clusters are believed to be at the same distance because of their similarities in kinematics.

Since these associations are young (4–5 Myr for Cyg OB2 – Wright et al. 2015; 1–3 Myr for Car OB1 – Hur et al. 2012), the signatures of their formation process may still remain detectable in the kinematics as well as in the internal structure. To find evidence of the formation process of OB associations, we probe the spatial distribution and kinematics of high-mass stars in Cyg OB2 and Car OB1. The data we used are described in Section 2. The internal structure and kinematics of Cyg OB2 and Car OB1 are explored in Sections 3 and 4, respectively. We discuss their formation process in Section 5. Finally, our results are summarised in Section 6.

2 DATA

The census of high-mass stars (O-, B-type stars, and Wolf-Rayet stars) in Cyg OB2 and Car OB1 associations is more complete than those of the low-mass star population. Such high-mass stars are brighter than $G \sim 16$ mag, and the *Gaia* DR2 provides very high precision astrometric data in that magnitude range (Gaia Collaboration et al. 2018). Therefore, we considered only the high-mass star population of the associations in this study. For Cyg OB2, a list of high-mass stars compiled by Wright et al. (2015) was used. This catalogue contains the spectral types, the stellar parameters, and the photometric data of 167 stars earlier than B5 taken from a number of references. For Car OB1, Nazé et

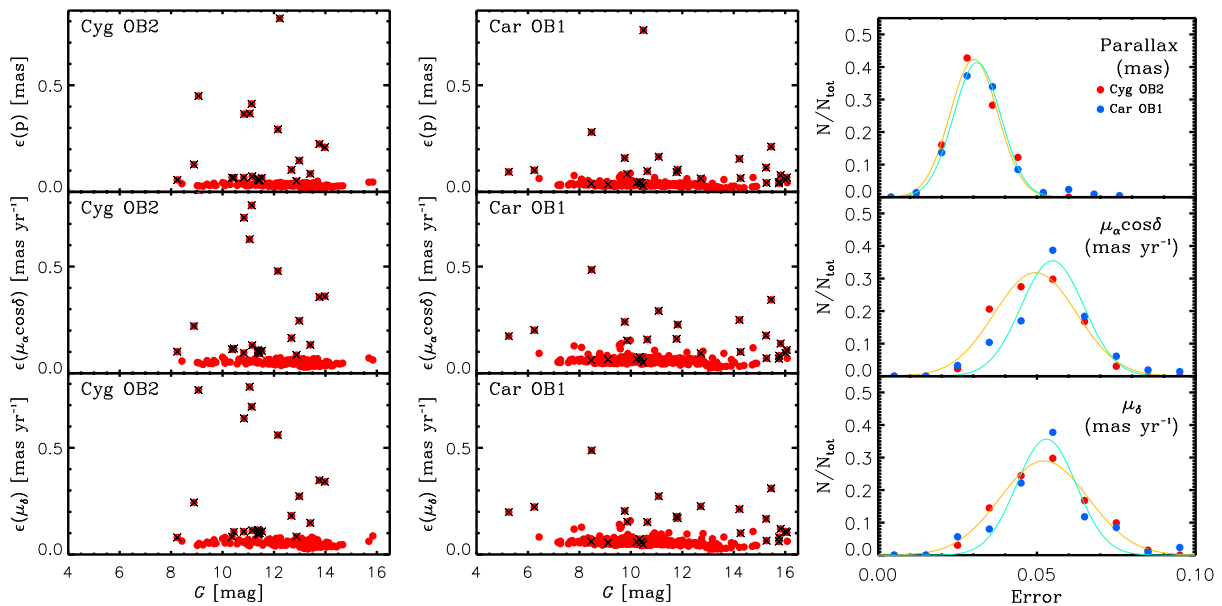


Figure 1. Error distributions of parallaxes and PMs with respect to the G band magnitude for stars in Cyg OB2 and Car OB1. In the left and middle panels, crosses represent either the data with errors larger than three times the standard deviation from the mean of errors in parallax and PM or those with parallaxes smaller than five times the associated parallax errors. These data were not used in further analysis. The right-hand panel displays the normalised number distributions of errors in parallax and PM that we used in this paper. Red and blue dots represent the data for Cyg OB2 and Car OB1, respectively.

al. (2011) studied 200 OB stars [70 O-type and 130 B-type, compiled from Skiff (2009)]. In addition, we added 106 OB stars from recent photometric or spectroscopic studies (Hur et al. 2012; Sota et al. 2014; Alexander et al. 2016; Damiani et al. 2017; Hanes et al. 2018). A total of 306 high-mass stars in Car OB1 were included in the final list.

The parallaxes and PMs of these stars in these associations were taken from *Gaia* DR 2 (Gaia Collaboration et al. 2018). The counterparts of those OB stars were searched for within $2''0$ in the *Gaia* catalogue. We found 165 and 304 counterparts for Cyg OB2 and Car OB1, respectively. Fig. 1 displays the errors in parallaxes and PMs with respect to G magnitude. In some cases, the catalogue of *Gaia* DR2 includes parallaxes and PMs with large errors. We did not use the data with errors larger than three times the standard deviation from the mean of the errors in parallax and PM. The errors in parallaxes and PMs used in this work are, on average, about 0.03 mas and 0.05 mas yr $^{-1}$, respectively. Since the standard deviations of errors are small (about 0.01 mas for parallax and 0.01 mas yr $^{-1}$ for PMs), the astrometric data of all stars considered in our study are subject to very similar errors. The mean of errors were used as a typical error. Stars with negative parallaxes or close companions (duplication flag = 1) were also excluded. In addition, stars with parallaxes smaller than five times their associated errors were excluded from further analysis. We present the full catalogues of our sample stars in Tables 1 and 2, respectively.

In this study, the distance to a given association is determined from the mode value of the distance distribution of members. Exclusion of negative or very small parallaxes can bias the true distribution of distances particularly for remote objects (Lindgren et al. 2018). The distance to our targets can then be underestimated by the sample truncation as a mode value of the distance distribution of members

is expected to be shifted to a smaller distance. To examine its effect on the derived distances, the distance distributions of stars were obtained by the inversion of the *Gaia* parallaxes from the full and truncated samples, respectively, and compared with each other. The mode values of these two distributions appeared at almost the same distance (less than 10 pc difference). This may be because all members of these associations are concentrated in small areas relative to their distances. Hence, our sample truncation scheme does not significantly influence the distances determined in the present work.

A zero point problem in the *Gaia* DR2 parallaxes has been raised. Lindgren et al. (2018) estimated a small zero point offset of -0.03 mas from the parallax distribution of quasars, while Stassun & Torres (2018) reported a somewhat larger offset of -0.08 mas in the zero point from comparison of the parallaxes of known eclipsing binaries with those of the *Gaia* mission. In addition, Zinn et al. (2019) found a moderate offset of -0.05 mas from the asteroseismology of red clump stars. These studies indicate that the parallaxes measured from the *Gaia* mission seem to be slightly underestimated. In this paper, we considered the three different zero point offsets as well as the case without correction for these offsets. Accordingly, the mean of errors in parallaxes increases up to 0.05 mas as a result of the quadratic sum of the typical error (0.03 mas) and the errors of the zero point offsets.

In order to probe the kinematic properties of stars in substructures, we used the amplitude of a global PM vector defined as below:

$$\mu = \sqrt{\mu_{\alpha}^2 \cos^2 \delta + \mu_{\delta}^2} \quad (1)$$

The orientation of PMs was also expressed by the position

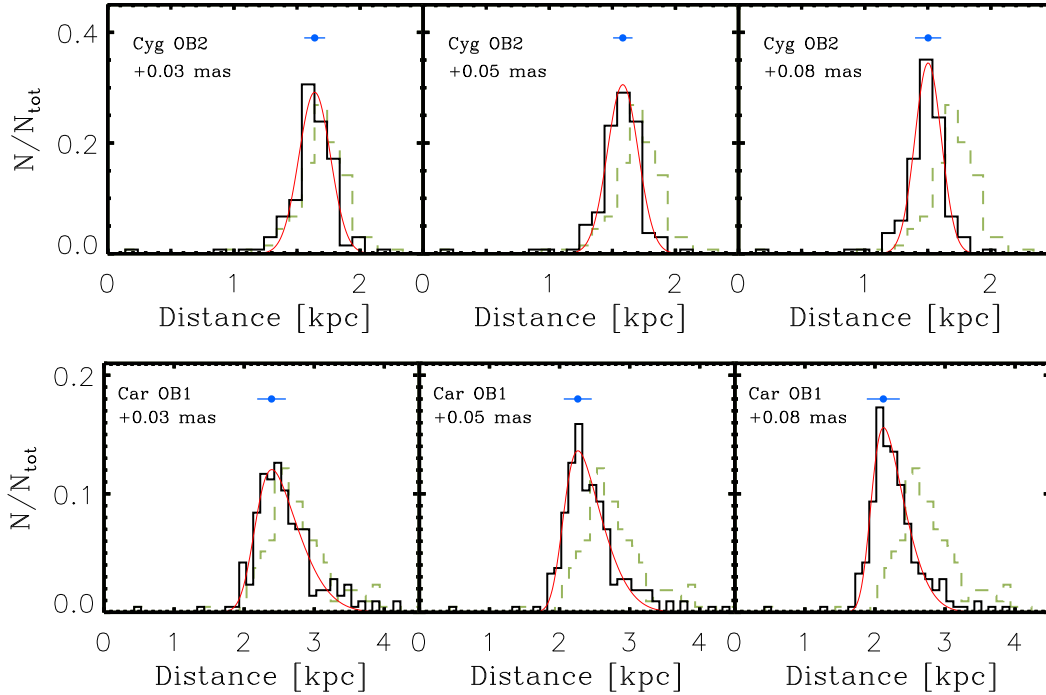


Figure 2. Distance distributions of stars in the direction of Cyg OB2 (upper) and Car OB1 (lower). The zero point offsets of 0.03, 0.05, and 0.08 mas were applied to the parallaxes of *Gaia* DR2 (Lindgren et al. 2018; Stassun & Torres 2018; Zinn et al. 2019). Histograms (light green) outlined by light green dashed lines exhibit the distributions of distances without correction for the zero point offsets. All the histograms were obtained with a bin size of about 0.1 kpc. The error bar at the top of each panel represents the mean of errors in distance. In order to find peak distances, Gaussian and skewed Gaussian profiles were fitted to the histograms for Cyg OB2 and Car OB1, respectively (red solid lines). In this paper, a mean value obtained from the peak distances (and indicated by the blue dot) was adopted as the distance to a given association.

angles (Φ) of PM vectors. The errors on these parameters were propagated from the errors in PMs.

3 INTERNAL STRUCTURE

Prior to probing the internal structures of these possible associations, we need to check whether or not these are a line-of-sight coincidence of several stellar groups. For this purpose, we computed the distances to individual stars from the inversion of the *Gaia* DR2 parallaxes. Fig. 2 exhibits the distance distributions of our sample stars in the direction of the two associations. The different systematic offsets were applied to the parallaxes in each case. In the case of Cyg OB2, the distributions of distance appear to be nearly Gaussian. The distance to Cyg OB2 was estimated to be 1.6 kpc with a standard deviation of 0.1 kpc. A systematic error of ± 0.1 kpc can be considered for this result because of the zero point offsets in parallax. This result is in reasonable agreement with those derived from previous studies (Hanson 2003; Rygl et al. 2012). The width of parallax distribution is governed by two terms, the intrinsic scatter (radial extent) and the scatter due to measurement errors, i.e., $\sigma_{\text{obs}} = \sqrt{\sigma_{\text{extent}}^2 + \sigma_{\text{error}}^2}$. Typical distance errors converted from the parallax errors (0.03 – 0.05 mas) are comparable to the standard deviation (0.1 kpc). This fact implies that the extent of this association along the line-of-sight is smaller than 200 pc.

On the other hand, the distance distributions of stars

in the direction of Car OB1 have a long tail towards larger distances. A fit by skewed Gaussian profiles yields a peak distance of about 2.3 kpc. Systematic errors of ± 0.2 kpc can be considered for the result. Car OB1 is located towards the tangent of the Sagittarius-Carina spiral arm, and therefore several background OB stars could be observed in the direction of this association. In order to check whether or not the stars further away than 3 kpc are background stars, we investigated the distribution of *Gaia* parallaxes. As a result, it appears to be a single Gaussian profile, not a skewed Gaussian profile, which implies that the asymmetric distribution at large distance comes from the inversion of the parallax to obtain distance (Bailer-Jones et al. 2018). The results obtained from the peaks in the parallax [0.412 ± 0.035 (sys.) mas] which is equivalent to 2.4 ± 0.2 (sys.) kpc] and distance distributions are consistent within the systematic errors. The Gaussian width is about 0.05 mas, which is equivalent to 0.3 kpc. If we adopt a typical error of 0.03 mas, the radial size of Car OB1 is then about 420 pc. However, this is an upper limit because the distribution of parallaxes can be entirely governed by the uncertainties if the error on the systematic error (0.03 mas) from Stassun & Torres (2018) is considered.

Such a large extent can be understood in the context of star formation. Indeed, the young open cluster NGC 281 and two H₂O maser sources, IRAS 00259+5625 and IRAS 00420+5530, are part of an expanding ring of molecular clouds, the so-called Megeath’s ring (Megeath et al. 2002,

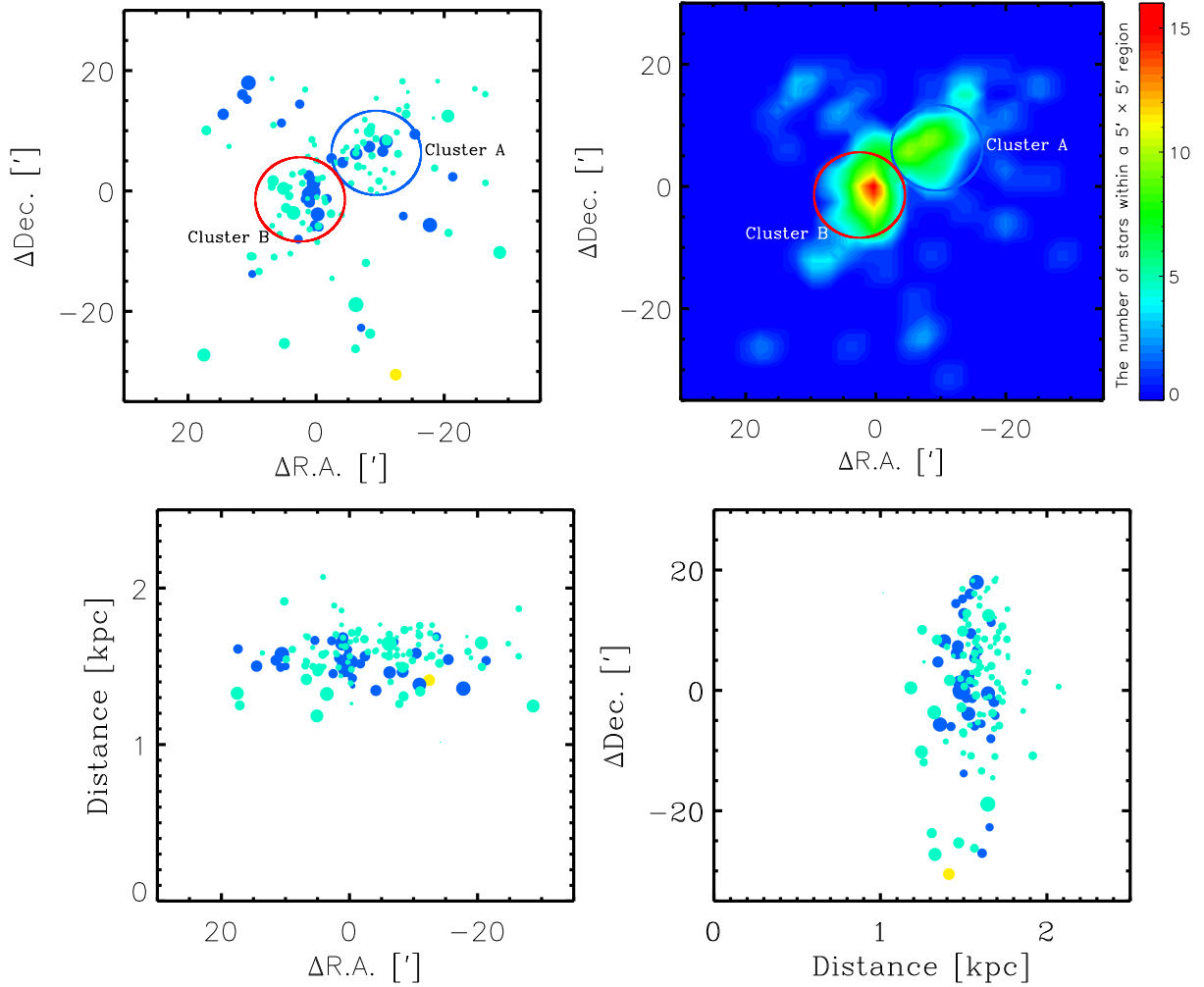


Figure 3. Distribution of stars in Cyg OB2. Upper left-hand panel: Spatial distribution of stars. The blue and red circles exhibit the position of Cluster A and Cluster B, respectively. Upper right-hand panel: Stellar surface density. The number of stars was counted within areal bins of $5' \times 5'$. Lower left-hand and lower right-hand panels display the distribution of distances to stars with respect to right ascension and declination, respectively. The positions of stars are relative to R.A. = $20^{\text{h}} 33^{\text{m}} 12^{\text{s}}.00$, Dec. = $41^{\circ} 19' 1''.2$ (J2000). Blue, cyan, and yellow dots represent O-, B-type, Wolf-Rayet stars, respectively. The size of dots are proportional to the brightness of stars. A moderate offset of -0.05 mas (Zinn et al. 2019) was applied to the parallaxes of stars to obtain their distances.

2003). Their parallaxes measured by using Very Long Baseline Interferometry Exploration of Radio Astrometry indicate that the three objects are lying along the line-of-sight (see figure 4 in Sato et al. 2008 and figure 5 in Sakai et al. 2014). The diameter of the expanding ring derived from the distance difference among them is about 0.7–1.9 kpc (Sato et al. 2008). This result implies that star formation can take place on a scale of several hundred parsecs. Our result naturally explains the discrepancy in distance among different studies of Car OB1 (2.2–2.9 kpc, Allen & Hillier 1993; Smith 2006; Hur et al. 2012).

There are a few foreground OB stars at $d < 1.0$ kpc and at $d < 1.7$ kpc in the direction of Cyg OB2 and Car OB1, respectively. A probable background star towards Cyg OB2 was also found. We list these OB star candidates in Table 3 and do not use them in further analysis. Except for these stars, most of the other OB stars are located in the same star forming complex, and therefore Cyg OB2 and Car OB1 are real stellar systems not chance alignments.

Figs. 3 and 4 display the spatial distribution of high-mass stars in those associations, respectively. The positions of stars are relative to R.A. = $20^{\text{h}} 33^{\text{m}} 12^{\text{s}}.00$, Dec. = $41^{\circ} 19' 1''.2$ (J2000) for Cyg OB2 and R.A. = $10^{\text{h}} 45^{\text{m}} 3^{\text{s}}.55$, Dec. = $-59^{\circ} 41' 3''.95$, (J2000) for Car OB1. In Cyg OB2, there are two groups of stars with a high-stellar density at $(\Delta\alpha, \Delta\delta) \sim (-9'.4, 6'.3)$ and $(2'.5, -1'.4)$. A low-density halo extending up to about $20'$ surrounds these clusters. The presence of these three substructures is confirmed in the surface stellar density map (upper right-hand panel of Fig. 3), where the number of stars was counted within areal bins of $5' \times 5'$. The western and eastern groups contain up to 10 and 16 OB stars per areal bin (1.85 and 2.95 OB stars pc^{-2}), respectively, while the halo encompasses about 0.3 ± 0.7 OB stars per areal bin (0.06 OB stars pc^{-2}) on average. The peak number density of OB stars in these groups are at least 30 times higher than that of the halo. Hereafter, the western and eastern clusters are referred to as Cluster A and Cluster B, respectively.

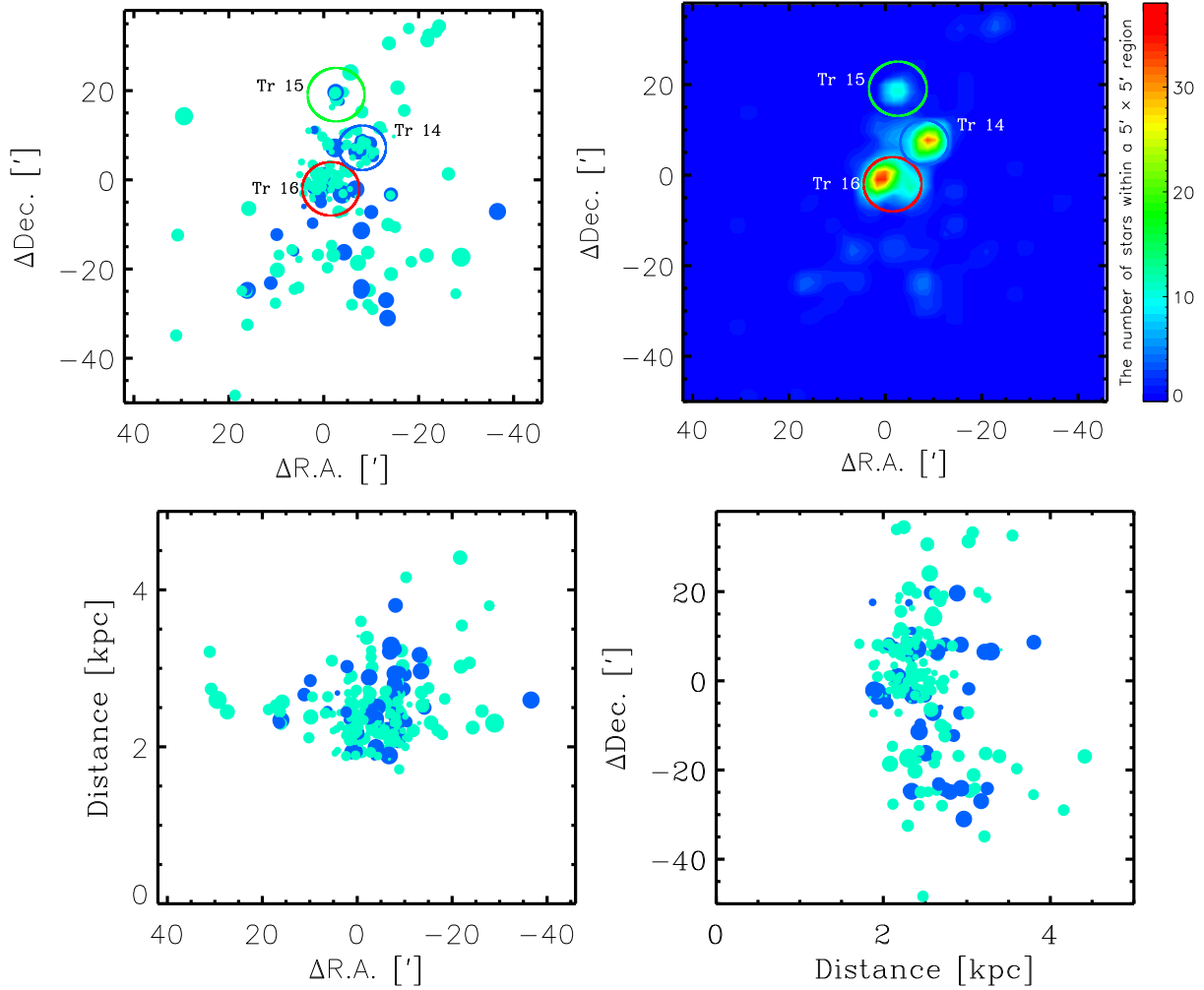


Figure 4. Distribution of stars in Car OB1. The positions of stars are relative to η Car (R.A. = $10^{\text{h}} 45^{\text{m}} 3^{\text{s}}.55$, Dec. = $-59^{\circ} 41' 3''.95$, J2000). The description of each panel and the other symbols are the same as in Fig. 3. The blue, green, and red open circles in the upper left-hand panel show the positions of the core clusters Tr 14, 15, and 16, respectively.

In Car OB1, several star clusters are distributed over this association (Feigelson et al. 2011). Tr 14, 15, and 16 among them appear as the most prominent cases, due to their abundant high-mass star content (see also upper right-hand panel of Fig. 4). A low-density halo also surrounds the entire association and extends to $30'$ along right ascension and declination axes. These clusters contain up to 36, 13, and 38 OB stars within the areal bin (3.22 , 1.16 , and 3.40 OB stars pc^{-2}), respectively, while the mean stellar density of the halo is about 0.3 ± 0.9 OB stars per areal bin (0.03 OB stars pc^{-2}). For early-type stars, the peak number densities of these clusters are similar to those of the clusters in Cyg OB2. Note that the number densities of OB stars obtained in this work may be a lower limit because later B-type stars and stars with a duplication flag in the *Gaia* catalogue were not used in this analysis.

A common property of both associations is that they consist of a few high-density core clusters and a low-density halo. This structural feature was also seen in other associations, such as Cep OB3, Ori OB1, Lac OB1, and Cas OB6 (Blaauw 1964; Koenig et al. 2008; Sung et al. 2017). This

feature could then be a relic of the formation of OB associations, which would imply that there may be a common process controlling their formation.

4 KINEMATIC SUBSTRUCTURES

In order to better characterise the formation process of these associations, we probe the kinematics of each substructure. In this section, the criteria of member selection are addressed, and the overall properties of individual substructures are described using the distributions of μ , Φ , and RVs of members.

4.1 Cyg OB2

Fig. 5 displays the distributions of the μ and Φ of stars in Cyg OB2 with respect to right ascension and declination. Most of the stars are moving in the μ range of 4 mas yr^{-1} to 6 mas yr^{-1} . In order to select the probable members of Cluster A and Cluster B, we first use the regions assigned to these clusters as shown in the upper left-hand panel of

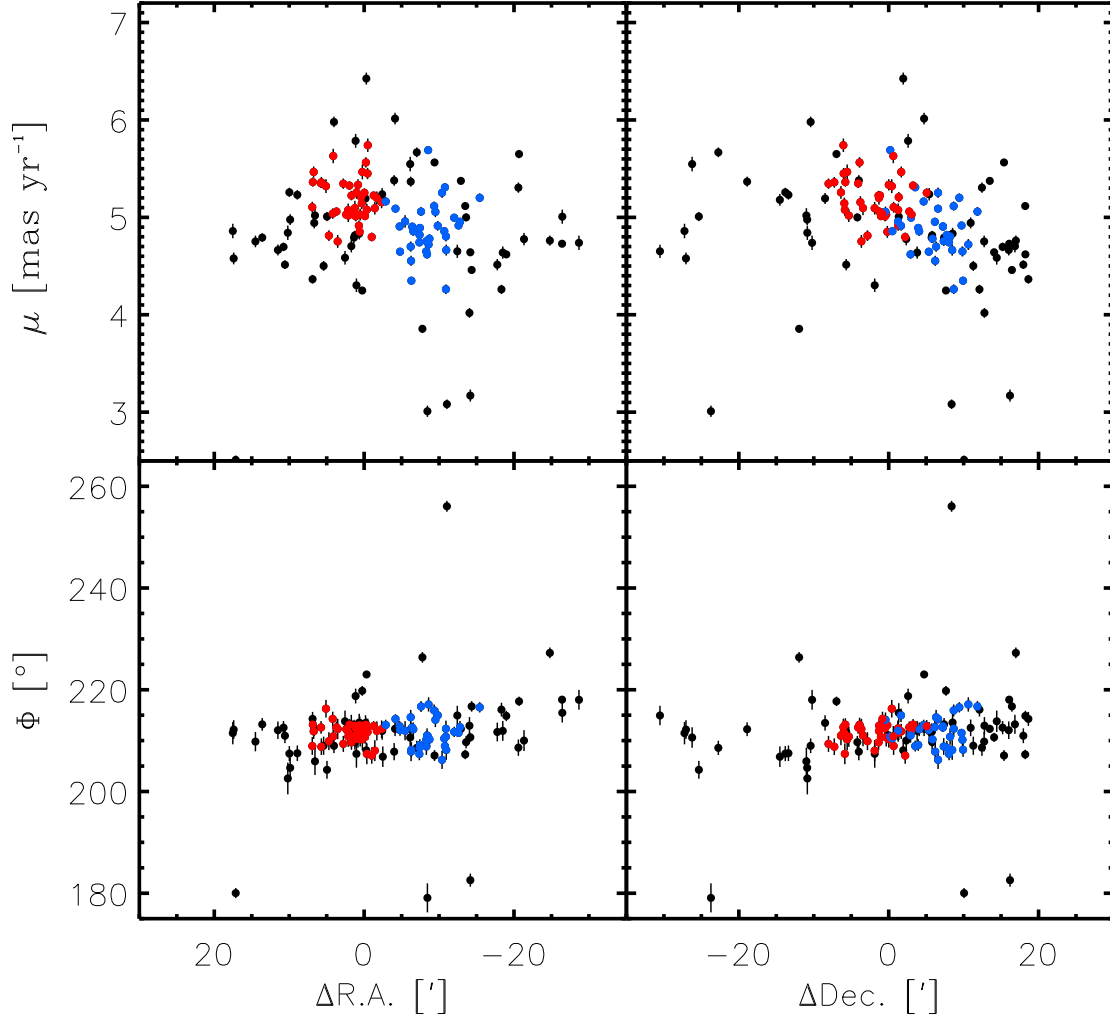


Figure 5. PM distributions of stars in Cyg OB2. Upper panels display the amplitude of PMs (μ) with respect to right ascension and declination, respectively, while lower panels exhibit the orientations of PMs (Φ) along each equatorial coordinate. Blue, red, and black dots represent Cluster A, Cluster B, and the halo stars, respectively.

Fig. 3, where the centre positions and radii of the regions were visually set to include as many probable cluster members as possible from the spatial distribution of stars. Note that the positions and radii used in the criteria are thus not the physical centre and size of these clusters. The μ and Φ of stars in different regions were then plotted in Fig. 5 by different colours. Stars with μ and Φ values within three times the standard deviations from the mean values were selected as members of given clusters. The criteria for membership to Cluster A and Cluster B are:

(i) Cluster A – R.A. = $20^{\text{h}}32^{\text{m}}21^{\text{s}}.89$,
Dec. = $+41^{\circ}25'20''.8$, J2000,
radius = $7'$

(ii) Cluster B – R.A. = $20^{\text{h}}33^{\text{m}}25^{\text{s}}.31$,
Dec. = $+41^{\circ}17'37''.2$, J2000,
radius = $7'$

(iii) $\langle\mu\rangle - 3\sigma_{\mu} < \mu < \langle\mu\rangle + 3\sigma_{\mu}$

(iv) $\langle\Phi\rangle - 3\sigma_{\Phi} < \Phi < \langle\Phi\rangle + 3\sigma_{\Phi}$

where $\langle\mu\rangle$, σ_{μ} , $\langle\Phi\rangle$, and σ_{Φ} represent the mean values and standard deviations in μ and Φ for a given cluster. These values were iteratively computed until outliers were completely removed from the subsample. Stars not satisfying these criteria were considered as the halo stars. The numbers of members in Cluster A, Cluster B, and the halo are 33, 39, and 59, respectively.

The centre and size of each substructure were determined using the selected members. The centre positions of each substructure quoted in Table 4 were obtained from the median coordinates of the selected members. It is worth noting that these centre positions well match those used in the criteria for member selection. In practice, it is difficult to define the area of the substructures, particularly the extent of the halo. Here, the largest distances among members in the clusters and halo were adopted as their maximum diameters for simplicity. The diameters of Cluster A, Cluster B, and the halo are 6.2 ± 0.4 , 6.3 ± 0.4 , and 28.7 ± 1.8 pc at 1.6

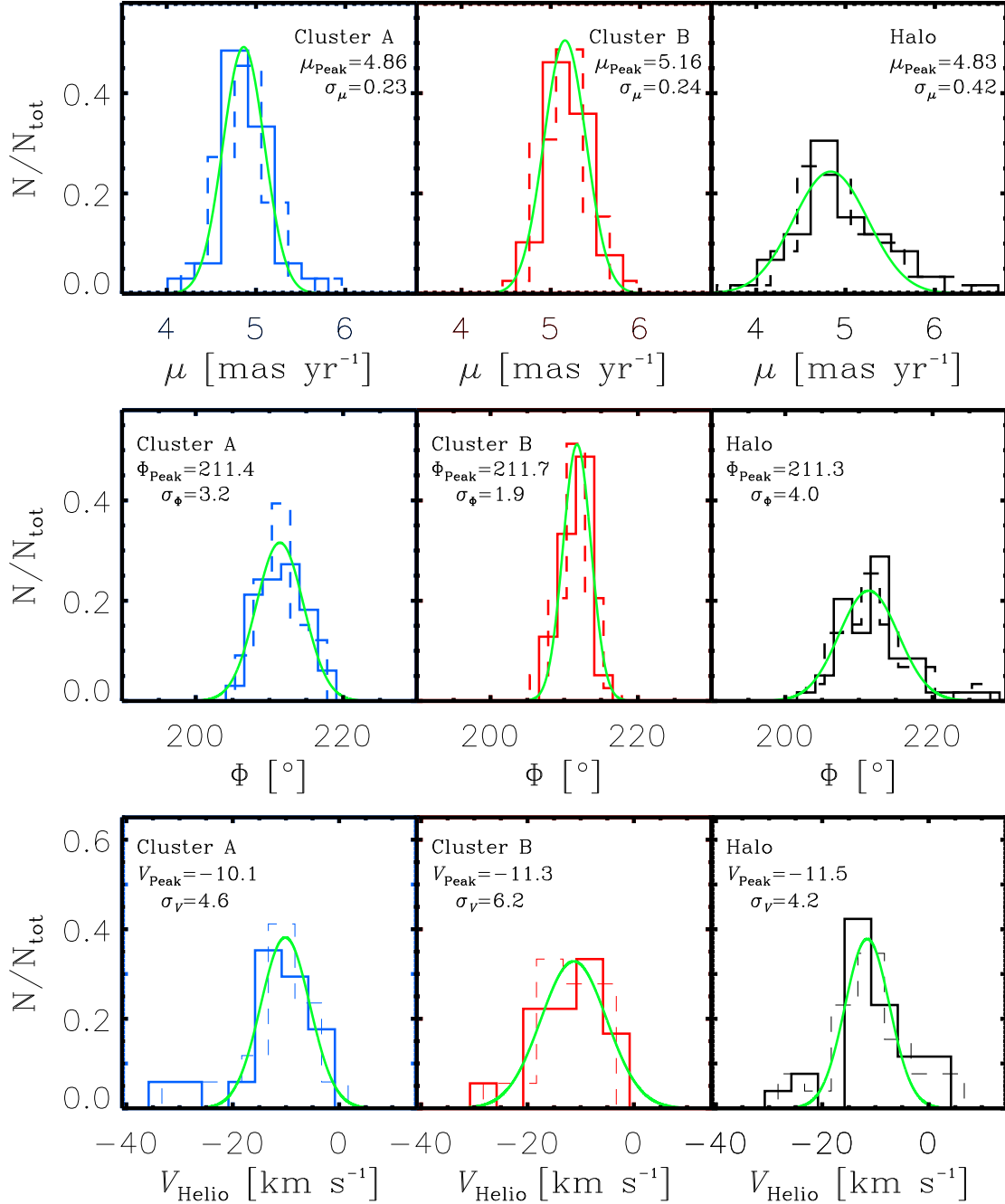


Figure 6. Distributions of PMs and RVs of stars in Cyg OB2. Bin sizes of 0.3 mas yr^{-1} , 2.5° , and 5 km s^{-1} were adopted for obtaining each distribution. Two histograms are presented, based on two positions for bin centres (solid and dashed lines), to show the impact of the binning. The names of stellar groups and the best-fit parameters are labelled at the top of each panel. The curves drawn by green solid lines are the best-fit Gaussian distributions.

kpc, respectively, where their errors were propagated from the systematic errors on distance.

These clusters have slightly different amplitudes in PM. The members of Cluster A have μ values in the range of 4.2 to 5.8 mas yr^{-1} , and the μ values of the Cluster B members are confined between 4.7 and 5.8 mas yr^{-1} . The orientations of their PMs appear to be globally well aligned at about 210° . It means that the star clusters and the halo stars are globally moving towards almost the same direction.

The upper and middle panels of Fig. 6 exhibit the μ

and Φ distributions of stars belonging to Cluster A, Cluster B, and halo, respectively. They were fitted by Gaussian profiles, and the best solutions (the mean and dispersion) are quoted in each panel. The global PM of Cluster A appears smaller than that of Cluster B. The difference is about 0.30 mas yr^{-1} (equivalent to 2.3 km s^{-1}), which is larger than three times the mean of errors (0.05 mas yr^{-1}). Stars in the halo are moving, on average, at 4.83 mas yr^{-1} , which is similar to that of Cluster A but they have a dispersion almost twice larger than those found for Cluster A and Cluster B.

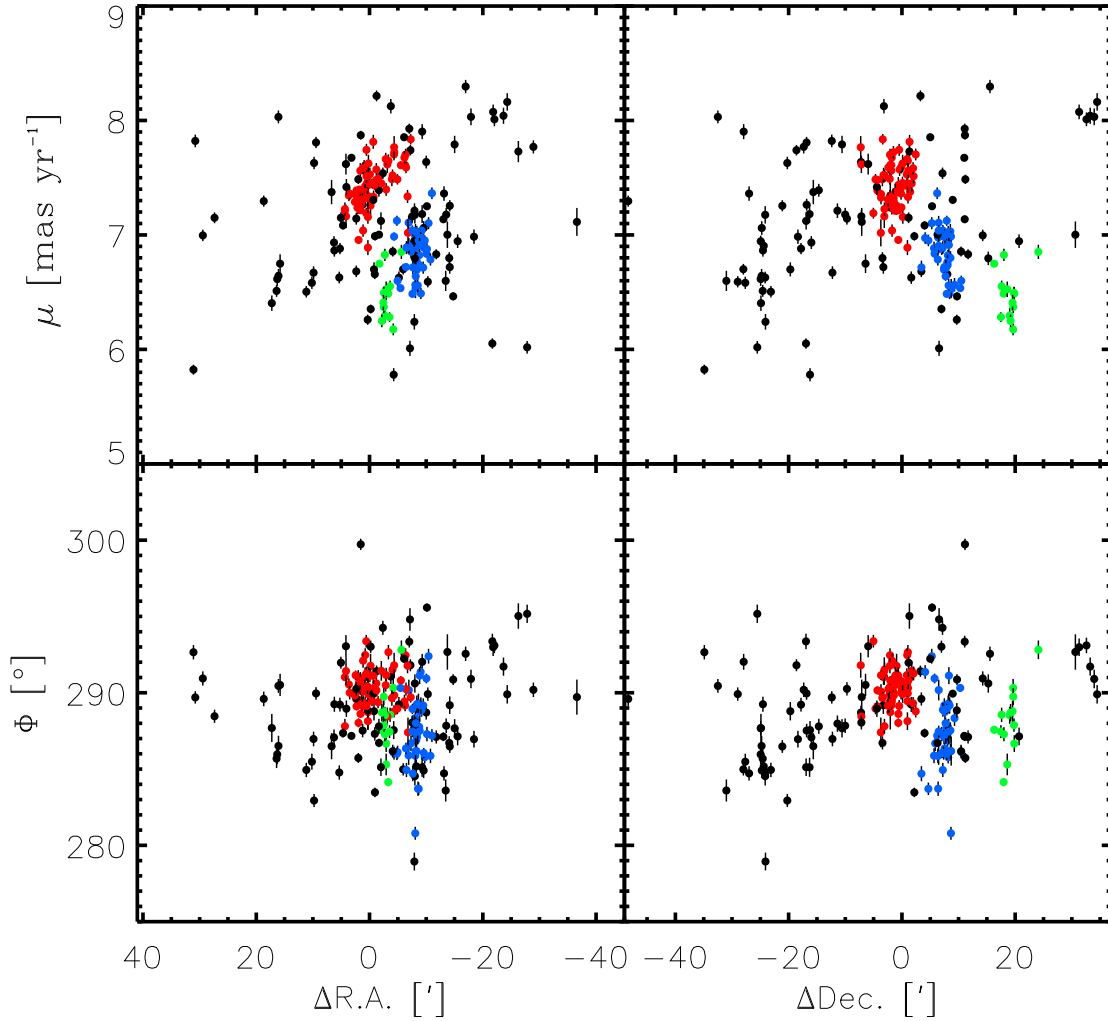


Figure 7. PM distributions of stars in Car OB1. Blue, green, red, and black dots represent Tr14, 15, 16, and the halo stars, respectively.

Similarly, the halo is presenting a larger dispersion in Φ . Together with the large dispersion in μ , this may indicate that the halo stars suffer from larger contributions from random motions than stars in Cluster A and Cluster B.

We further probed the kinematic substructures of Cyg OB2 along the line of sight by using the RVs of 61 out of 102 stars in Kiminki et al. (2007). Spectroscopic binary stars (26) and binary candidates (15) were not used. The lower panels of Fig. 6 display the RV distribution of stars in Cluster A, Cluster B, and halo, respectively. The mean RVs and dispersions were obtained by the Gaussian profile fitting to each RV distribution. The RVs of stars in the substructures seem not to be significantly different from each other: Cluster A, Cluster B, and the halo have mean RVs of -10.1 , -11.3 , and -11.5 km s^{-1} with different dispersions of 4.6, 6.2, and 4.2 km s^{-1} , respectively. If Cluster A and Cluster B have isotropic velocity components in the three-dimensional space, the velocity difference between these clusters along the line-of-sight is about 1.6 km s^{-1} (or $V_{2D} = \sqrt{2}V_{1D} = 2.3$ km s^{-1} , where V_{1D} and V_{2D} are a one-dimensional velocity and two-dimensional velocity calculated from $\Delta\mu \times$ distance, respectively). Because of the large velocity dispersions, it would be difficult to strongly argue that this differ-

ence can be detected in the RV distributions despite the fact that the RV difference between these clusters is about 1 km s^{-1} . We present the overall properties of the substructures in Cyg OB2 in Table 4.

4.2 Car OB1

Fig. 7 displays the distributions of the μ and Φ of OB stars in Car OB1 with respect to their positions. The PMs of these stars range from 5.5 mas yr^{-1} to 8.3 mas yr^{-1} in μ , and between 276° and 300° in Φ . The kinematics of stars is well correlated with the positions of stars. In the same way as for Cyg OB2, we first selected the probable members of Tr 14, 15, and 16 within three circular regions as below (see the upper left-hand panel of Fig. 4);

- (i) Tr 14 – R.A. = $10^{\text{h}}43^{\text{m}}59^{\text{s}}.59$,
Dec. = $-59^{\circ}33'51''.9$, J2000,
radius = 5'
- (ii) Tr 15 – R.A. = $10^{\text{h}}44^{\text{m}}43^{\text{s}}.14$,
Dec. = $-59^{\circ}21'57''.9$, J2000,

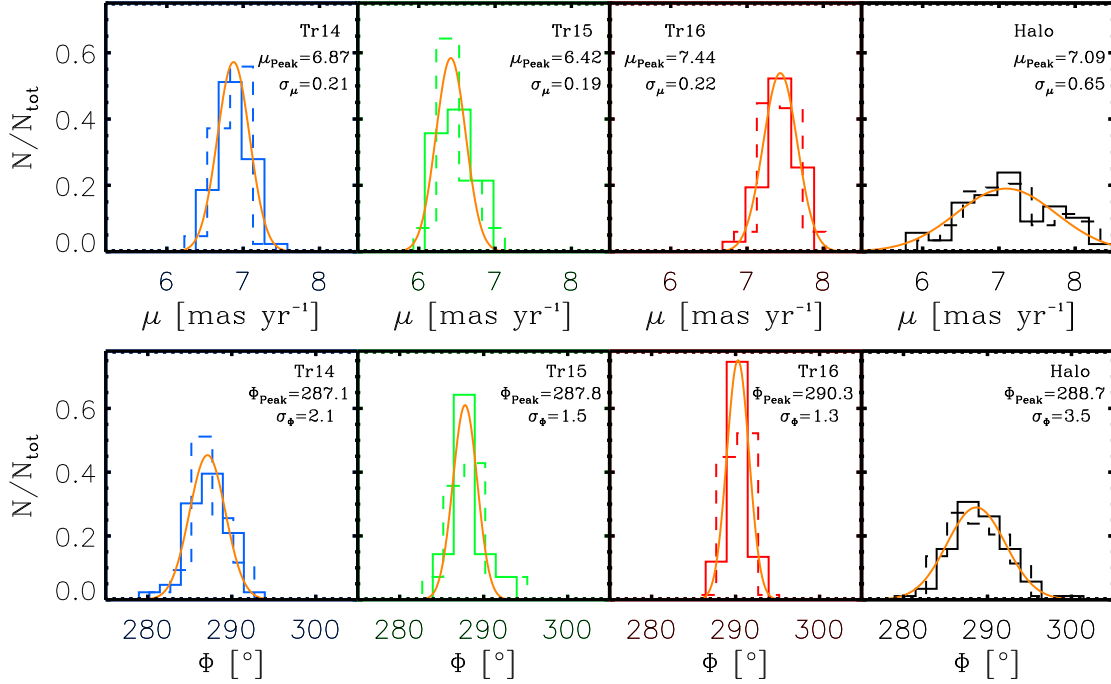


Figure 8. Distributions of PMs of stars in Car OB1. The bin sizes of 0.3 mas yr^{-1} and 2.5° were adopted for obtaining each distribution. The names of stellar groups and the best-fit parameters are displayed at the top of each panel. The curves drawn by orange solid lines are the Gaussian distributions adopting the best-fit parameters.

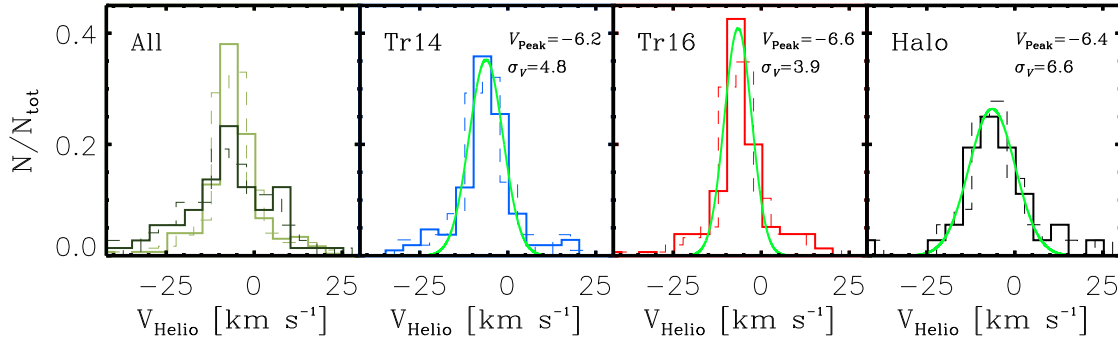


Figure 9. Distributions of RVs of stars in Car OB1. A bin size of 5 km s^{-1} was adopted for obtaining each distribution. In the left-hand panel, dark and light histograms display the RV distributions of OB stars and late-type stars from Damiani et al. (2017) in the entire region, respectively. The other panels exhibit the RV distributions of low-mass stars in each cluster (except Tr 15) or the halo. The green curves represent the best-fit Gaussian distributions.

$$\text{radius} = 6'$$

- (iii) Tr 16 – R.A. = $10^{\text{h}}44^{\text{m}}51^{\text{s}}.65$,
 Dec. = $-59^{\circ}43'03''.9$, J2000,
 radius = $6'$

The μ and Φ of stars are plotted in Fig. 7 by different colours. Stars with μ and Φ values within three times the standard deviations from the cluster mean values were selected as members (see the criteria iii and iv used for Cyg OB2). Stars not fulfilling these criteria were assumed to form the halo population. The numbers of members in Tr14, 15, 16, and the halo are 43, 14, 67, and 88, respectively. Note that several OB stars of the other clusters, such as Bochum 10, 11,

Collinder 232, and 228, may be included in this halo population because we only considered the most prominent clusters Tr 14, 15, and 16 in this paper. The centre positions of these clusters given in Table 4 were also adopted from the median coordinates of members. The maximum diameters of Tr 14, 15, 16, and the halo were determined to be 5.1 ± 0.5 , 5.8 ± 0.5 , 7.9 ± 0.7 , and 68.9 ± 6.0 pc at 2.3 kpc, respectively, from the maximum distances among the members.

Fig. 8 displays the distributions of the μ and Φ of stars in the three clusters and the halo. The best solutions from Gaussian fitting to each distribution are labelled in each panel. Tr 15 has the smallest μ (6.42 mas yr^{-1}), while Tr 16 has the largest value (7.44 mas yr^{-1}). The μ values of the three clusters seem to vary with declination (see the upper

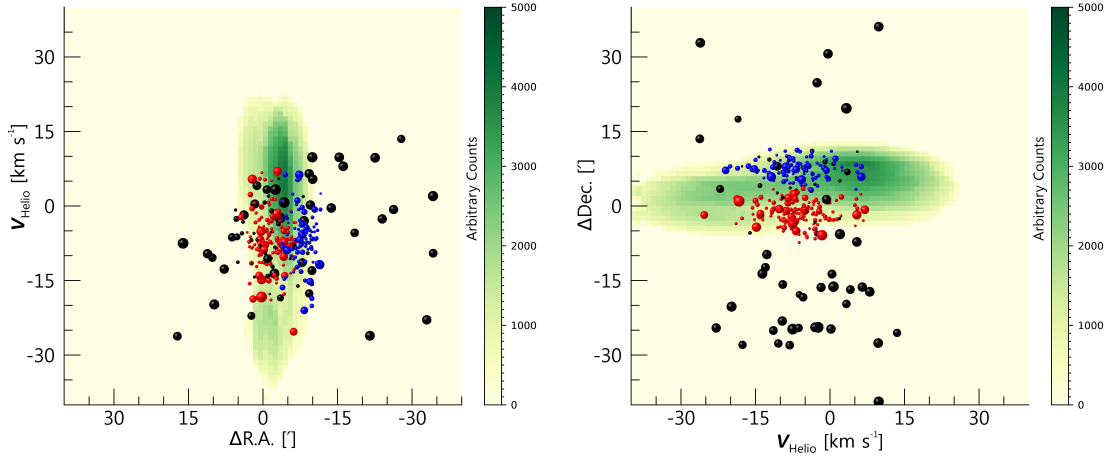


Figure 10. Position-velocity diagrams of ionised gas and stars along right ascension (left) and declination (right). The distribution of ionised gas was traced by the forbidden line $[\text{N II}] \lambda 6584$. Red, blue, and black spheres denote the members of Tr 14, 16, and the halo, respectively, and their size is proportional to the brightness of individual stars in the G band.

right-hand panel of Fig. 7). It is also interesting that these clusters have almost the same dispersion (about 0.2 mas yr^{-1}) in μ . On the other hand, the halo stars have a global PM of 7.09 mas yr^{-1} with a larger dispersion (0.65 mas yr^{-1}) than those of the clusters. Given the typical error of 0.05 mas yr^{-1} , this difference in kinematics is a true feature.

Tr 14 ($287^\circ 1$), 15 ($287^\circ 8$), and 16 ($290^\circ 3$) have similar orientations of PMs. Again, the star clusters have smaller dispersions ($1^\circ 3 - 2^\circ 1$) than the halo stars ($3^\circ 5$), implying that the members of the clusters have globally well-aligned motions towards given directions.

In 2013 and 2014, Hanes et al. (2018) observed a total of 115 OB stars spread over Car OB1 and measured their RVs. We took their weighted mean values for the same stars, where the inverse of the squared error was used as the weight value. Some known binary stars were excluded in this analysis. Only a total of 19 and 54 OB stars for three clusters and the halo are available in this paper, respectively. This number is insufficient to statistically investigate their kinematics, particularly for the clusters. For this reason, we used the RVs of low-mass stars later than A2 derived by Damiani et al. (2017). Note that the low-mass stars in Tr 15 were not observed in their study. The boundaries of Tr 14 and 16 (see above) were used to distinguish the members of these two clusters. The left-hand panel of Fig. 9 compares the RVs of OB stars with those of late-type stars. These stars have almost the same mean velocities, -6.9 ± 11.5 (s.d.) km s^{-1} for OB stars and -6.4 ± 4.5 (s.d.) km s^{-1} for late-type stars. The RV distribution of OB stars appears broader than that of late-type stars. This is because the measurement errors ($\langle \epsilon_{\text{RV}} \rangle = 6.5 \text{ km s}^{-1}$) for OB stars are larger than those ($\langle \epsilon_{\text{RV}} \rangle = 4.6 \text{ km s}^{-1}$) for late-type stars on average.

The other panels of Fig. 9 display the RV distribution of late-type stars in Tr 14, 16, and the halo. The mean RVs of these two clusters obtained from the best-fit Gaussian profiles are about -6.2 and -6.6 km s^{-1} , respectively. Those values are not significantly different given the fact that the

errors on RVs are larger than the discrepancy: these clusters are thus moving at almost the same velocities along the line-of-sight. The halo stars are moving at -6.4 km s^{-1} , on average, which is also close to the mean RVs of Tr14 and 16. However, their velocity dispersion (6.6 km s^{-1}) again appears larger than those of the clusters (4.8 km s^{-1} for Tr 14 and 3.9 km s^{-1} for Tr 16).

Spectroscopic observations of ionised gas across the Carina nebula were carried out by Damiani et al. (2016). Their observations allow us to compare the kinematics of stars and gas. The optical spectra of the ionised gas show double-peaked emission lines of various elements. They provided the best-fit solutions for the line profiles, such as RVs, velocity dispersions, and counts. We reconstructed a total of 297 synthetic nebular spectra of the forbidden line $[\text{N II}] \lambda 6584$ from the best-fit solutions at various nebular positions. Subsequently, this information on fibre positions and line profiles was interpolated to a regular grid consisting of $80 \times 80 \times 80$ cells by applying Delauney triangulation technique as done in Lim et al. (2018). Two-dimensional position-velocity diagrams were then obtained by summing the counts along right ascension or declination (Fig. 10), respectively. OB and late-type stars with RVs within three times the mean of errors from the mean value are also plotted in these diagrams.

The ionised gas of the Carina nebula surrounds Tr 14 and 16 with a shell-like appearance in position-velocity space as expected from the double-peaked nature of the emission lines (Damiani et al. 2016). Our sample stars are located between the two shell structures. The RV distribution of stars and gas supports our claim that these clusters are in the same association. The near-side of the ionised shell is moving towards us in the RV range of -15 km s^{-1} to -35 km s^{-1} , while the RVs of its far-side range from 0 km s^{-1} to 20 km s^{-1} . The median RV of each shell was compared with the mean RV of stars. As a result, the ionised shell appears to be globally expanding away from the Tr 14 and

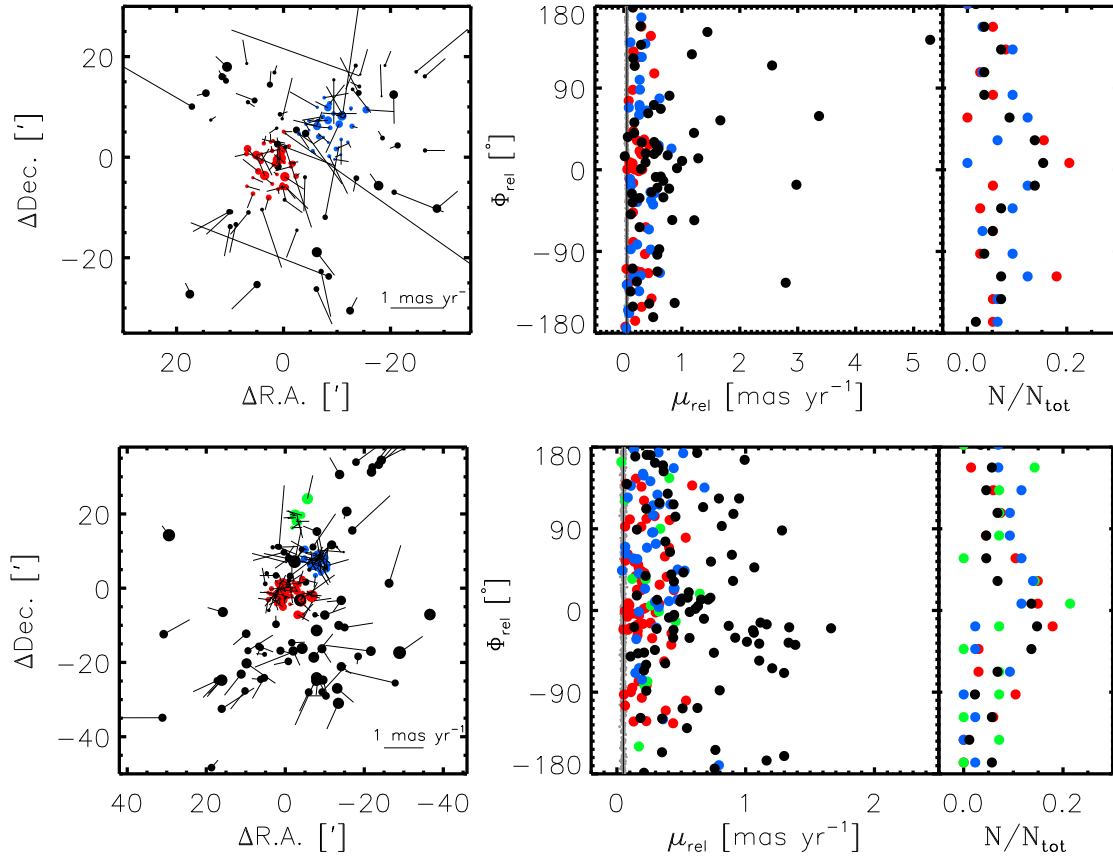


Figure 11. Relative PM vectors of stars in Cyg OB2 (upper) and Car OB1 (lower). Left panels : spatial distributions of OB stars and their relative PMs. The size of dots is proportional to the brightness of individual stars in the *G* band. Straight lines display the PM vectors relative to the median PMs of given substructures. Right panels : distribution of μ_{rel} and Φ_{rel} . The different colours indicate stars in clusters (red, blue, green) or in halos (black). The vertical solid line indicates the typical error in μ_{rel} . Simulated distributions are shown by grey dots. The side panels display the distribution of Φ_{rel} , where the histograms were normalised by the total number of members belonging to each substructure.

16 clusters at about 17 km s^{-1} . The overall properties of the substructures in Car OB1 are summarised in Table 4.

5 SIGNATURE OF FORMATION PROCESS

We tested whether or not these associations were formed by expansion of single or multiple star clusters. For this purpose, the amplitude of PM vectors (μ_{rel}) relative to the median PMs of given clusters or halos was defined as follows;

$$\mu_{\text{rel}} = \sqrt{(\mu_{\alpha} \cos \delta - \mu_{\alpha, \text{med}} \cos \delta_{\text{med}})^2 + (\mu_{\delta} - \mu_{\delta, \text{med}})^2} \quad (2)$$

where the subscript ‘med’ denotes the median PMs of given substructures. Φ_{rel} was also defined as the angle between the radial vector of a star from the centre position of a given substructure and its relative PM vector. Φ_{rel} values of stars should be distributed around 0° if the substructures are expanding, while the values may appear at either positive or negative 180° in the case of overall contraction.

Fig. 11 displays the distributions of relative PMs of stars in Cyg OB2 and Car OB1. In the left-hand panels, PM vectors seem to indicate some expanding motions of the halo stars. In the right-hand panels, the distributions are shown

in more detail. For Cyg OB2, the Φ_{rel} of Cluster A (shown in blue) appear spread out while those of the halo stars (in black) and of Cluster B (in red) display a peak near zero, indicating a contribution from radial expanding motion. In Car OB1, results are similar : Tr 14 (in blue) does not show any clear sign of expansion whereas Tr 15 (in green), Tr 16 (in red), and the halo (in black) seem to have a true low-level expansion.

Using a Monte-Carlo method, we tested whether or not μ_{rel} values are dominated by the measurement errors of the *Gaia* DR2. The errors in μ are distributed as a Gaussian profile with a standard deviation of 0.01 mas yr^{-1} centered at 0.05 mas yr^{-1} . A total of 1000 artificial stars were generated, and the errors drawn from this error distribution were assigned to the μ_{rel} of these stars. The Φ_{rel} values of these stars were randomly generated between -180° and 180° . As a result, the mean values of μ_{rel} for the substructures in Cyg OB2 and Car OB1 are greater than three times the mean value of the simulated μ_{rel} over all the directions (see grey dots in the right panel of Fig. 11). This simulation therefore seems to indicate the existence of several components in kinematics such as low-level expansion, intrinsic random motions of stars, and rotation of clusters.

Subgroups of stars in a number of OB associations were

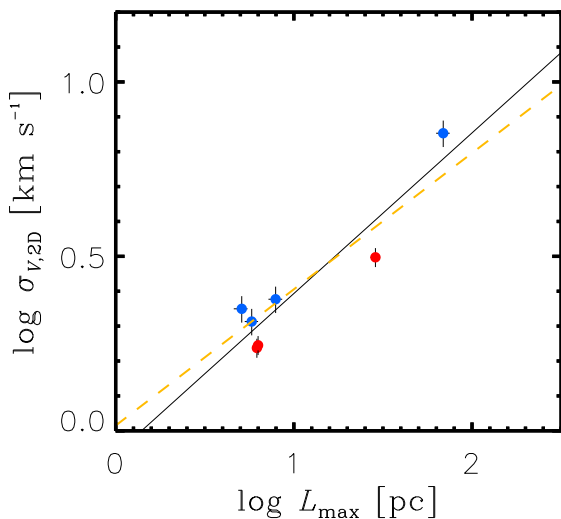


Figure 12. Correlation between the two-dimensional (2D) velocity dispersions and the maximum size of substructures. Red and blue dots represent the substructures of Cyg OB2 and Car OB1, respectively. The systematic errors in distance were propagated into the 2D velocity dispersions and the size of substructures, respectively. The solid line (black) displays the result of a linear regression [$\log \sigma_{v,2D} = 0.46(\pm 0.08) \log L_{\max} - 0.07(\pm 0.09)$], and the dashed line (orange) shows a linear relation [$\log \sigma_{v,2D} = 0.39 \log L_{\max} + 0.02$] estimated from the Theil-Sen estimator.

found to be expanding (Mel’nik & Dambis 2017; Kounkel et al. 2018; Kuhn et al. 2019). Some of the substructures in Cyg OB2 and Car OB1 also reveal kinematic properties similar to those of the unbound associations. If crossing time of stars is shorter than or comparable to their age, the model invoking expansion of clusters after rapid gas expulsion (Tutukov 1978; Hills 1980; Lada et al. 1984; Kroupa et al. 2001; Goodwin & Bastian 2006) could explain the formation of Cyg OB2 and Car OB1. The μ dispersions of star clusters are only about 0.2 mas yr^{-1} . The halo extends to at least $20'$ from each star cluster. The crossing time of stars for this angular distance is about 6 Myr. This timescale is longer than the age of stars (4–5 Myr for Cyg OB2 – Wright et al. 2015; and 1–3 Myr for Car OB1 – Hur et al. 2012). It implies that the formation of these two associations cannot be fully explained by the cluster expansion. This is consistent with the conclusion of Wright et al. (2014, 2016) although they could not find any signature of expansion.

On the other hand, supersonic turbulence plays an important role in the formation of hierarchical substructures in gravitationally bound molecular clouds (Larson 1981). Recent *Herschel* observations showed that nearby molecular clouds form a network of filamentary structures (André 2015). It seems that turbulent flows may be responsible for this structure formation (Padoan et al. 2001). Once the turbulence is dissipated by shocks, clouds may have different sizes and velocity dispersions according to their virial states. This is observed as a relation between the velocity dispersions and the size of clumps and molecular clouds, i.e. $\sigma \propto L^\alpha$, where α ranges from 0.3 to 0.5 (Larson 1981; Snell 1981, etc). Clark et al. (2005) successfully reproduced structures in OB associations by applying this relation to their smoothed particle hydrodynamics simulations for star

formation in gravitationally unbound clouds. If hierarchical star formation driven by turbulence is a more preferable explanation than the dynamical evolution of stellar systems, then the observed structures and kinematics of OB associations should be similar to those of molecular clouds.

We thus investigated the relation between velocity dispersions and sizes of the substructures. The two-dimensional (2D) velocity dispersions ($\sigma_{v,2D}$) of the substructures were obtained by σ_μ multiplied by distance. The errors on $\sigma_{v,2D}$ were propagated from the systematic errors in distance. The maximum diameters of each substructure determined in Section 4 were adopted. Interestingly, Fig. 12 reveals a possible correlation between the 2D velocity dispersions and the maximum size of substructures in Cyg OB2 and Car OB1. We determined the slope of the correlation using a least-square fitting method and found that the velocity dispersions follow a relation $\sigma_{v,2D} \propto L_{\max}^{0.46 \pm 0.08}$. The slope of this correlation was also estimated using a Theil-Sen estimator, leading to a value of 0.39. These two results are consistent with each other within the error, and the derived trend is similar to that found in molecular clouds. Star formation in turbulent and globally unbound clouds may therefore be a better explanation than the expansion of clusters for the formation of Cyg OB2 and Car OB1 (see also the review of Gouliermis 2018). However, the number of the identified substructures is insufficient to reach a definite conclusion in the current state. A systematic survey for more OB associations will be able to identify a number of substructures and to confirm this relation. Nevertheless, our results are supported by the fact that Kuhn et al. (2019) also found a signature of a positive correlation between one-dimensional velocity dispersions and half-mass radii of star clusters in different OB associations.

6 SUMMARY

We studied the internal structure and kinematics of the two OB associations Cyg OB2 and Car OB1 in the Galaxy using the high-precision astrometric data from *Gaia* DR2 (Gaia Collaboration et al. 2018) and RVs from previous studies (Kiminki et al. 2007; Damiani et al. 2017; Hanes et al. 2018). From the distribution of distances, we concluded that these associations are genuine structures rather than a line-of-sight coincidence of several stellar groups. They were found to comprise dense core clusters and a sparse halo as seen in other OB associations. These substructures reveal different kinematic properties from each other in PM. Star clusters with small extent (5 – 8 parsecs) tend to have small dispersions in both amplitude (μ) and orientation (Φ) of PM, while the halo stars, spread over a few tens of parsecs, reveal larger dispersions. We also probed the RV distributions of stars in each substructure. Stars in Cyg OB2 do not show significant differences between clusters and halo in RV. In Car OB1, the velocity dispersion of the halo stars appears larger than those of stars within clusters, as for their PM distributions.

The relative PMs of stars in star clusters and halo showed that some of these substructures reveal a weak signature of expansion. However, the expansion of clusters cannot fully explain the formation of these associations given the large crossing time of stars, which is longer than their ages.

Instead, a correlation between the sizes and velocity dispersions of the substructures was found, which is reminiscent of the “size-line width” relation of molecular clouds (Larson 1981). If this correlation was inherited from that of natal clouds, these associations might have formed in turbulent giant molecular clouds. However, because of small number statistics, this correlation should be confirmed by identifying more substructures in other associations and enlarging the sample size from the forthcoming *Gaia* data.

ACKNOWLEDGEMENTS

The authors thank the anonymous referee for many constructive comments. This work has made use of data from the European Space Agency (ESA) mission *Gaia* (<https://www.cosmos.esa.int/gaia>), processed by the *Gaia* Data Processing and Analysis Consortium (DPAC, <https://www.cosmos.esa.int/web/gaia/dpac/consortium>). Funding for the DPAC has been provided by national institutions, in particular the institutions participating in the *Gaia* Multilateral Agreement. This work was supported by the National Research Foundation of Korea (NRF) grant funded by the Korea government (MSIT) (Grant No: NRF-2019R1C1C1005224), Basic Science Research Program through the NRF funded by the Ministry of Education of Korea (Grant No. NRF-2017R1A6A3A03006413), and BK 21 plus program through the NRF funded by the Ministry of Education of Korea. YN, EG, and GR also acknowledge support by the FNRS and by Belspo through the PRODEX contracts.

REFERENCES

- Alexander, M. J., Hanes, R. J., Povich, M. S., McSwain, M. V. 2016, *AJ*, 152, 190
- Allen, D. A., Hillier, D. J., 1993, *Proceedings of the Astronomical Society of Australia*, 10, 338
- Ambartsumian, V. A. 1947, In *Stellar Evolution and Astrophysics*, Armenian Acad. of sci. (German translation, 1951, *Abhandl. Sowjetischen Astron.*, 1, 33)
- André, P. 2015, *HiA*, 16, 31
- Bailer-Jones, C. A. L., Rybizki, J., Foesneau, M., Mantelet, G., Andrae, R. 2018, *AJ*, 156, 58
- Baumgardt, H., Kroupa, P. 2007, *MNRAS*, 380, 1589
- Berlanas, S. R., Wright, N. J., Herrero, A., Drew, J. E., Lennon, D. J. 2019, *MNRAS*, 484, 1838
- Blaauw, A. 1964, *ARA&A*, 2, 213
- Bonnell, I. A., Smith, R. J., Clark, P. C., Bate, M. R. 2011, *MNRAS*, 410, 2339
- Bresolin, F., Kennicutt, R. C. Jr., Stetson, P. B. 1996, *AJ*, 112, 1009
- Briceño, C., Preibisch, T., Sherry, W. H., et al. 2007, *Protostars and Planets V*, 345
- Cantat-Gaudin, T., et al. 2018, preprint (arXiv:1812.08114)
- Clark, P. C., Bonnell, I. A., Zinnecker, H. & Bate, M. R. 2005, *MNRAS*, 359, 809
- Comerón, F., et al. 2002, *A&A*, 389, 874
- Cudworth, K. M., Martin, S. C., Degioia-Eastwood, K. 1993, *AJ*, 105, 1822
- Damiani, F., et al. 2016, *A&A*, 591, A74
- Damiani, F., et al. 2017, *A&A*, 603, A81
- Elmegreen, B. G. 2002, *ApJ*, 577, 206
- Elmegreen, B. G. 2008, *ApJ*, 672, 1006
- Feigelson, E. D., et al. 2011, *ApJS*, 194, 9
- Gaia Collaboration et al. 2016, *A&A*, 595, A1
- Gaia Collaboration et al. 2018, *A&A*, 616, A1
- Garcia, M. et al. 2009, *A&A*, 502, 1015
- Goodwin, S. P., Bastian, N. 2006, *MNRAS*, 373, 752
- Gouliermis, D. A. 2018, *PASP*, 130, 072001
- Hanes, R. J., McSwain, M. V., Povich, M. S. 2018, *AJ*, 155, 190
- Hanson, M. M. 2003, *ApJ*, 597, 957
- Hills, J. G. 1980, *ApJ*, 235, 986
- Hur, H., Sung, H., Bessell, M. S. 2012, *AJ*, 143, 41
- Johnson, H. L., & Morgan, W. W. 1954, *ApJ*, 119, 344
- Kiminki, D. C., et al. 2007, *ApJ*, 664, 1102
- Kiminki, M. M., Smith, N. 2018, *MNRAS*, 477, 2068
- Knödseder, J. 2000, *A&A*, 360, 539
- Koenig, X. P., Allen, L. E., Gutermuth, R. A., et al. 2008, *ApJ*, 688, 1142
- Kounkel, M., et al. 2018, *AJ*, 156, 84
- Kroupa, P., Aarseth, S., Hurley, J. 2001, *MNRAS*, 321, 699
- Kruijssen, J. M. D. 2012, *MNRAS*, 426, 3008
- Kuhn, M. A., et al. 2019, *ApJ*, 870, 32
- Lada, C., Lada, E. 2003, *ARA&A*, 41, 57
- Lada, C., Margulis, M., Dearborn, D. 1984, *ApJ*, 285, 141
- Larson, R. B. 1981, *MNRAS*, 194, 809
- Leisawitz, D., Bash, F. N., Thaddeus, P. 1989, *ApJS*, 70, 731
- Levato, H., Malaroda, S. 1982, *PASP*, 94, 807
- Lim, B., et al. 2018, *MNRAS*, 477, 1993
- Lindgren, L., et al., 2018, *A&A*, 616, A2
- Luri, X., et al. 2018, *A&A*, 616, A9
- Massey, P., Johnson, J. 1993, *AJ*, 105, 980
- Massey, P., Thompson, A. B. 1991, *AJ*, 101, 1408
- Megeath, S. T., Biller, B., Dame, T. M., et al. 2002, in *ASP Conf. Ser. 267, Hot Star Workshop III: The Earliest Stages of Massive Star Birth*, ed. P. A. Crowther (San Francisco: ASP), 257
- Megeath, S. T., Biller, B., Dame, T. M., et al. 2003, *Rev. Mex. Astron. Astrofis., Ser. Conf.*, 15, 151
- Mel'nik, A. M., Dambis, A. K. 2017, *MNRAS*, 472, 3887
- Michalik, D., Lindgren, L., Hobbs, D. 2015, *A&A*, 574, A115
- Miller, G. E., Scalo, J. M. 1978, *PASP*, 90, 506
- Morrell, N., Garcia, B., Levato, H. 1988, *PASP*, 100, 1431
- Nazé, Y., et al. 2011, *ApJS*, 194, 7
- Padoan, P., Juvella, M., Goodman, A. A., Nordlund, Å. 2001, *ApJ*, 553, 227
- Pietrzyński, G., Gieren, W., Fouqué, P., Pont, F. 2001, *A&A*, 371, 497
- Porras A., Christopher M., Allen L., Di Francesco J., Megeath S. T., Myers P. C., 2003, *AJ*, 126, 1916
- Preibisch, T., et al. 2011, *A&A*, 530, A34
- Regan, M. W., Wilson, C. D. 1993, *AJ*, 105, 499
- Rygl, K. L. J., et al. 2012, *A&A*, 539, A79
- Sakai, N., et al. 2014, *PASJ*, 66, 3
- Sato, M., et al. 2008, *PASJ*, 60, 975
- Skiff, B. A. 2009, *Catalogue of Stellar Spectral Classifications, VizieR Catalog B/mk/mktypes (Lowell Observatory)*, 1, 2023
- Smith, N. 2006, *ApJ*, 644, 1151
- Snell, R. L. 1981, *ApJS*, 45, 121
- Sota, A., Maíz Apellániz, J., Morrell, N. I., et al. 2014, *ApJS*, 211, 10
- Stassun, K. G., Torres, G. 2018, *ApJ*, 862, 61
- Sung, H., Bessell, M. S., Chun, M.-Y., et al. 2017, *ApJS*, 230, 3
- Tutukov, A. V. 1978, *A&A*, 70, 57
- Ward, J. L., Kruijssen, J. M. D. 2018, *MNRAS*, 475, 5659
- Walborn, N. R. 1973, *ApJ*, 179, 517
- Walborn, N. R. 1995, *RevMexAA, Conf. Ser.*, 2, 51
- Walborn, N. R., et al. 2002, *AJ*, 123, 2754
- Wright, N. J., et al. 2016, *MNRAS*, 460, 2593
- Wright, N. J., Drake, J. J., Drew, J. E., Vink, J. S. 2010, *ApJ*, 713, 871

- Wright, N. J., Drew, J. E., Mohr-Smith, M. 2015, MNRAS, 449, 741
Wright, N. J., Mamajek, E. E. 2018, MNRAS, 476, 381
Wright, N. J., Parker, R. J., Goodwin, S. P., Drake, J. J. 2014, MNRAS, 438, 639
Zinn, J. C., Pinsonneault, M. H., Huber, D., Stello, D. 2018, ApJ, 878, 136Z

Table 1. Catalogue of high-mass stars in Cygnus OB2.

Sq.	α_{J2000} (h m s)	δ_{J2000} ($^{\circ}$ ' ")	Spectral Type	p (mas)	$\epsilon(p)$ (mas)	$\mu_{\alpha} \cos \delta$ (mas yr $^{-1}$)	$\epsilon(\mu_{\alpha} \cos \delta)$ (mas yr $^{-1}$)	μ_{δ} (mas yr $^{-1}$)	$\epsilon(\mu_{\delta})$ mas yr $^{-1}$	Dup ²	G (mag)	$\epsilon(G)$ (mag)	B_p (mag)	$\epsilon(B_p)$ (mag)	R_p (mag)	$\epsilon(R_p)$ (mag)	$B_p - R_p$ (mag)
1	20:32:03.10	+41:15:19.9	WC4	0.5355	0.0510	-2.619	0.085	-4.157	0.084	0	12.8727	0.0004	14.3121	0.0046	11.6628	0.0015	2.6493
2	20:32:06.29	+40:48:29.7	WN7 α /CE+O7V((f))	0.6555	0.0415	-2.664	0.066	-3.813	0.069	0	10.6348	0.0010	12.0984	0.0027	9.4580	0.0023	2.6404
3	20:35:47.10	+41:22:44.7	WC6+O8III	0.8345	0.3676	-2.916	0.628	-3.875	0.786	0	11.0537	0.0008	13.0142	0.0056	9.6917	0.0033	3.3225
4	20:33:08.78	+41:13:18.1	O3If+O6V	0.6231	0.0667	-2.685	0.095	-4.601	0.107	0	10.8262	0.0012	12.1324	0.0349	9.4787	0.0274	2.6538
5	20:33:14.16	+41:20:21.5	O3If	0.6248	0.0298	-2.724	0.051	-4.438	0.052	0	9.7405	0.0005	10.7503	0.0013	8.7606	0.0017	1.9897
6	20:33:18.02	+41:18:31.0	O5III	0.5544	0.0306	-2.687	0.046	-4.229	0.053	0	9.4794	0.0006	10.3727	0.0015	8.5614	0.0013	1.8112
7	20:33:10.74	+41:15:08.0	O5I+O3.5III	0.6012	0.0326	-3.041	0.045	-4.659	0.057	0	9.6060	0.0010	11.0193	0.0015	8.4582	0.0012	2.5611
8	20:34:08.55	+41:36:59.3	O5If+B0V	0.5810	0.0268	-2.322	0.041	-3.871	0.045	0	9.2414	0.0005	10.2712	0.0015	8.2541	0.0019	2.0172
9	20:33:23.46	+41:09:12.9	O5.5V	0.0000	0.0000	0.000	0.000	0.000	0.000	0	10.8943	0.0234	12.0022	0.0063	9.1825	0.0060	2.8197
10	20:33:13.25	+41:13:28.6	O6V	0.5694	0.0445	-2.754	0.072	-4.722	0.078	0	12.2473	0.0004	13.7639	0.0039	11.0366	0.0020	2.7273

Col. (1) : Sequential number. Cols. (2) and (3) : The equatorial coordinates of stars. Col. (4) : Spectral types of stars listed in Wright et al. (2015). Cols. (5) and (6) : Absolute parallax and its standard error. Cols. (7) and (8) : Proper motion in the direction of right ascension and its standard error. Cols. (9) and (10) : Proper motion in the direction of declination and its standard error. Col. (11) : Duplication flag. Cols. (12) and (13) : G magnitude and its standard error. Cols. (14) and (15) : B_p magnitude and its standard error. Cols. (16) and (17) : R_p magnitude and its standard error. Col. (18) : $B_p - R_p$ colour index. All the data listed from Col. (5) to Col. (18) were taken from Gaia DR2 (Gaia Collaboration et al. 2018).

The full table is available electronically.

Table 2. Catalogue of high-mass stars in Carina OB1.

Sq.	α_{J2000} (h m s)	δ_{J2000} ($^{\circ}$ $'$ $''$)	Spectral Type	p (mas)	$\epsilon(p)$ (mas)	$\mu_{\alpha} \cos \delta$ (mas yr $^{-1}$)	$\epsilon(\mu_{\alpha} \cos \delta)$ (mas yr $^{-1}$)	μ_{δ} (mas yr $^{-1}$)	$\epsilon(\mu_{\delta})$ mas yr $^{-1}$	Dup	G (mag)	$\epsilon(G)$ (mag)	B_p (mag)	$\epsilon(B_p)$ (mag)	R_p (mag)	$\epsilon(R_p)$ (mag)	$B_p - R_p$ (mag)
1	10:40:12.38	-59:48:09.7	O8V ¹	0.3322	0.0599	-6.697	0.121	2.400	0.128	0	8.0825	0.0032	8.1060	0.0100	8.0581	0.0094	0.0479
2	10:40:30.07	-59:56:51.1	B2III ¹	0.3042	0.0353	-6.922	0.059	3.105	0.064	1	10.5072	0.0004	10.5697	0.0012	10.3617	0.0010	0.2080
3	10:40:31.65	-59:46:43.6	B1.5III ¹	0.3784	0.0520	-6.909	0.093	2.961	0.087	1	8.7903	0.0004	8.7887	0.0016	8.7908	0.0015	-0.0021
4	10:40:39.22	-60:05:35.9	B2III ¹	0.2773	0.0470	-7.006	0.078	3.210	0.081	1	9.7862	0.0005	9.7513	0.0012	9.8430	0.0012	-0.0917
5	10:41:12.29	-59:58:24.7	B1.5II: ¹	0.3814	0.0327	-7.292	0.057	2.682	0.057	0	7.2207	0.0007	7.2199	0.0022	7.2386	0.0029	-0.0187
6	10:41:15.28	-59:57:45.2	B2Ib ¹	0.0698	0.0283	-5.694	0.051	2.666	0.047	0	10.4717	0.0004	10.7193	0.0010	10.0700	0.0009	0.6493
7	10:41:20.24	-60:06:36.1	B2V ¹	0.2103	0.0315	-5.447	0.056	2.560	0.052	0	11.1166	0.0010	11.1808	0.0046	10.9472	0.0027	0.2336
8	10:41:35.44	-59:39:44.8	B1.5V ¹	0.3543	0.0528	-7.003	0.092	3.270	0.094	0	9.8834	0.0004	9.9028	0.0018	9.8378	0.0017	0.0650
9	10:41:54.15	-59:06:36.3	B1V ¹	0.3925	0.0433	-7.675	0.076	2.778	0.077	0	9.6451	0.0005	9.6505	0.0012	9.6307	0.0012	0.0197
10	10:41:55.79	-59:16:16.4	B3III ¹	0.1678	0.0330	-7.231	0.064	3.316	0.069	1	9.7148	0.0007	9.7866	0.0022	9.5700	0.0019	0.2166

Col. (1) : Sequential number. Cols. (2) and (3) : The equatorial coordinates of stars. Col. (4) : Spectral types of stars obtained from previous studies, 1 – Nazé et al. (2011), 2 – Hur et al. (2012), 3 – Damiani et al. (2017), 4 – Sota et al. (2014), 5 – Alexander et al. (2016), 6 – Hanes et al. (2018). Cols. (5) and (6) : Absolute parallax and its standard error. Cols. (7) and (8) : Proper motion in the direction of right ascension and its standard error. Cols. (9) and (10) Proper motion in the direction of declination and its standard error. Col. (11) : Duplication flag. Cols. (12) and (13) : G magnitude and its standard error. Cols. (14) and (15) : B_p magnitude and its standard error. Cols. (16) and (17) : R_p magnitude and its standard error. Col. (18) : $B_p - R_p$ colour index. All the data listed from Col. (5) to Col. (18) were taken from Gaia DR2 (Gaia Collaboration et al. 2018). The full table is available electronically.

Table 3. List of foreground and background star candidates

Object	R.A. (2000) (h m s)	Dec. (2000) ($^{\circ}$ $'$ $''$)	Spectral type	ρ (mas)	$\epsilon(\rho)$ (mas)	$\mu_{\alpha} \cos \delta$ (mas yr $^{-1}$)	$\epsilon(\mu_{\alpha} \cos \delta)$ (mas yr $^{-1}$)	μ_{δ} (mas yr $^{-1}$)	$\epsilon(\mu_{\delta})$ (mas yr $^{-1}$)	G (mag)	$\epsilon(G)$ (mag)
Cyg OB2											
BD+40 4213	20:31:46.00	+41:17:27.1	O9.5I ¹	7.1921	0.0292	-32.407	0.050	-16.439	0.043	9.0181	0.0003
ALS 15161	20:33:10.34	+41:13:06.4	B0V ¹	1.0399	0.0459	5.728	0.062	-3.398	0.087	15.8433	0.0011
ALS 15175	20:33:14.34	+41:19:33.1	B5V ¹	0.1867	0.0363	-3.163	0.063	-5.056	0.066	13.5165	0.0003
Car OB1											
HD 303296	10:42:25.04	-59:09:24.5	B1Ve ²	0.6908	0.0690	-7.508	0.132	3.053	0.141	9.5535	0.0007
HD 93695	10:47:44.32	-59:52:30.9	B3V ²	2.3023	0.0630	-14.788	0.093	0.685	0.082	6.4318	0.0004

Col. (1) : Names of objects. Cols. (2) and (3) : The equatorial coordinates of stars. Col. (4) : Spectral types of stars obtained from previous studies, 1 – Wright et al. (2015) and 2 – Nazé et al. (2011). Cols. (5) and (6) : Absolute parallax and its standard error. Cols. (7) and (8) : Proper motion in the direction of right ascension and its standard error. Cols. (9) and (10) : Proper motion in the direction of declination and its standard error. Cols. (11) and (12) : G magnitude and its standard error. All the data listed from Col. (5) to Col. (12) were taken from Gaia DR2 (Gaia Collaboration et al. 2018).

Table 4. Properties of the substructures in Cygnus OB2 and Carina OB1.

Object	R.A. (2000) (h m s)	Dec. (2000) (° ' ")	N_{OB}	$\Sigma_{\text{Peak,OB}}$ (stars pc ⁻²)	$\langle\mu\rangle$ (mas yr ⁻¹)	σ_{μ} (mas yr ⁻¹)	$\langle\Phi\rangle$ (°)	σ_{Φ} (°)	RV (km s ⁻¹)	σ_{RV} (km s ⁻¹)	D (pc)	$\sigma_{V,2D}$ (km s ⁻¹)
Cyg OB2												
Cluster A	20:32:27.22	+41:25:36.4	33	1.85	4.86	0.23	211.4	3.2	-10.1	4.6	6.2 ± 0.4	1.7 ± 0.1
Cluster B	20:33:18.02	+41:17:44.9	39	2.95	5.16	0.24	211.7	1.9	-11.3	6.2	6.3 ± 0.4	1.8 ± 0.1
Halo	20:32:59.17	+41:23:44.9	59	0.06	4.83	0.42	211.3	4.0	-11.5	4.2	28.7 ± 1.8	3.1 ± 0.2
Car OB1												
Tr14	10:43:57.59	-59:33:28.1	43	3.22	6.87	0.21	287.1	2.1	-6.2	4.8	5.1 ± 0.5	2.2 ± 0.2
Tr15	10:44:42.31	-59:21:53.5	14	1.16	6.42	0.19	287.8	1.5			5.8 ± 0.5	2.1 ± 0.2
Tr16	10:45:05.84	-59:42:34.0	67	3.40	7.44	0.22	290.3	1.3	-6.6	3.9	7.9 ± 0.7	2.4 ± 0.2
Halo	10:44:30.96	-59:50:46.7	88	0.03	7.09	0.65	288.7	3.5	-6.4	6.6	68.9 ± 6.0	7.1 ± 0.6

Col. (1) : Names of objects. Cols. (2) and (3) : The equatorial coordinates of stars. Col. (4) : The number of members. Col. (5) : Peak number density of OB stars. Cols. (6) and (7) : Mean amplitude of proper motions and its dispersion. Cols. (8) and (9) : Mean orientation of proper motions and its dispersion. Cols. (10) and (11) : Mean radial velocities and its dispersion. Col. (12) : Maximum diameter. Col. (13) : Two-dimensional velocity dispersion.

This paper has been typeset from a $\text{T}_{\text{E}}\text{X}/\text{L}^{\text{A}}\text{T}_{\text{E}}\text{X}$ file prepared by the author.